Journal of Magnetic Resonance 201 (2009) 72–80

Contents lists available at ScienceDirect

Journal of Magnetic Resonance

journal homepage: www.elsevier.com/locate/jmr

Quantitative single point imaging with compressed sensing

P. Parasoglou [a], D. Malioutov [b], A.J. Sederman [a], J. Rasburn [c], H. Powell [c], L.F. Gladden [a], A. Blake [b], M.L. Johns [a,*]

[a] Department of Chemical Engineering and Biotechnology, University of Cambridge, New Museums Site Pembroke Street, Cambridge CB2 3RA, UK
[b] Microsoft Research Ltd., 7 J J Thompson Ave., Cambridge CB3 0FB, UK
[c] Nestec York Ltd., Nestlé Product Technology Centre, Haxby Road, P.O. Box 204, York YO91 1XY, UK

ARTICLE INFO

Article history:
Received 30 March 2009
Revised 23 July 2009
Available online 14 August 2009

Keywords:
Compressed sensing
SPI
Under-sampling
k-space

ABSTRACT

A novel approach with respect to single point imaging (SPI), compressed sensing, is presented here that is shown to significantly reduce the loss of accuracy of reconstructed images from under-sampled acquisition data. SPI complements compressed sensing extremely well as it allows unconstrained selection of sampling trajectories. Dynamic processes featuring short T_2^* NMR signal can thus be more rapidly imaged, in our case the absorption of moisture by a cereal-based wafer material, with minimal loss of image quantification. The absolute moisture content distribution is recovered via a series of images acquired with variable phase encoding times allowing extrapolation to time zero for each image pixel and the effective removal of T_2^* contrast.

© 2009 Elsevier Inc. All rights reserved.

1. Introduction

Single point imaging was originally proposed as a 'solid state' imaging modality [1,2]. As a pure phase-encoding imaging technique, SPI is relatively immune to artefacts due to chemical shift, magnetic susceptibility variations and inhomogeneities in the B_0 field [3,4] and has thus been extensively used to image samples with very short transverse relaxation time (T_2^*), of the order of 100 μs [5]. Typically these materials also have short spin–spin relaxation times (T_2) and thus frequency-encoding imaging techniques are unsuitable due to the minimum limits on the time for echo formation.

The difficulty of slice selection in SPI has confined its use predominantly to one or three dimensional imaging. Since only one point in ***k***-space (the acquired data which is subsequently Fourier transformed to produce an image) is typically sampled after each r.f. signal excitation, total acquisition times are long and in some cases prohibitive for the time resolution needed for certain applications. Several attempts have been made in the past in order to speed up acquisition, the most prominent being SPRITE, as developed by Balcom and co-workers [6]; this enables significantly faster acquisition as the phase encoding magnetic field gradients are ramped up in discrete steps as opposed to being switched on and off between each ***k***-space point acquisition.

Conventionally such SPI approaches have been performed by sampling ***k***-space in a linear raster starting at the extremities of ***k***-space. Centric scans that result in improved sensitivity, as well as removal of T_1 contrast, have however almost completely replaced this original sampling trajectory. Since a better signal to noise ratio (SNR) is achieved per scan, fewer repeat scans are needed in total to achieve a required SNR threshold. Centric scans with different geometrical functions such as spirals and square spirals [7,8] have appeared in the literature. As we have shown in a previous study [9], prior knowledge of the sample shape can enable the design of near optimum sampling trajectories, where the SNR is maximised by sampling ***k***-space points with the highest expected value convolved with the largest excited magnetization. Note that SPI, as a pure phase-encoding imaging pulse sequence, has the desirable feature of placing no constraints on the sampling trajectory.

Since imaging speed is important in MRI applications, many researches have focused on acquiring only a portion of ***k***-space without significantly degrading the image quality. Traditionally in centric scans which employ spiral acquisitions, the extremities of ***k***-space are under-sampled and the values are replaced by zeros before reconstructing the image with the use of the Fourier transform. When all ***k***-space points as dictated by the desired field of view (*FOV*) and spatial resolution are not sampled, the Nyquist sampling theorem is theoretically violated. In this case the reconstructed images are expected to show artefacts and diminished accuracy if reconstructed by a linear transform (such as the Fourier transform). Compressed sensing (*CS*) has shown the ability to reconstruct images which are significantly under-sampled

* Corresponding author. Tel.: +44 1223 334767; fax: +44 1223 334796.
E-mail address: mlj21@cheng.cam.ac.uk (M.L. Johns).

1090-7807/$ - see front matter © 2009 Elsevier Inc. All rights reserved.
doi:10.1016/j.jmr.2009.08.003

[10,11] with minimal loss of quantification. This image reconstruction method takes advantage of the fact that certain transformations of MR images such as wavelet or spatial differences are typically very sparse. Sparsity in this transform domain allows good reconstruction from an under-sampled set of measurements in ***k***-space. Lustig et al. [11], studied the exploitation of sparsity of MR (conventional frequency-phase encoded) images in a transform domain and proposed a non-linear iterative reconstruction of the under-sampled images based on l_1-optimization which results in minimal loss of image quality/quantification.

In the work presented here, moisture absorption from humidified air by a thin cereal-based wafer material is considered. A 2D and a 3D binary MR image of the wafer sample is shown in Fig. 1(a) and (b), respectively. Such moisture absorption (and subsequent migration within the wafer foam) occurs during an industrial conditioning process. The conditioning process is required in order to optimise the expansion properties of the wafer for subsequent fabrication steps during confectionery production. Hence this process has a significant contribution to the final quality of the product. Temporally resolved MRI of such a system is very challenging. The wafer is highly porous (typically 80–90 vol%) while the absorbed moisture ranges from 1 to 20 wt% of the solid content. This low moisture content occurs as 'bound' water with restricted mobility; the porous nature of the wafer also results in significant magnetic susceptibility variations. These collectively result in a short T_2^* for the water, typically of the order of 100 μs, whilst T_1 remains relatively long (~1 s). Imaging the system with conventional MRI frequency-encode methods is not possible, hence the use of SPI.

To follow the dynamic moisture absorption process by the wafer, the following approach was developed and implemented: SPI was implemented in 3D with an under-sampled acquisition of 33% of ***k***-space. The sampling trajectory was optimised based on the expected amplitude of the points in ***k***-space as outlined in our previous publication [9]. Reconstruction of the images from this acquired ***k***-space data is achieved via a non-linear iteration (based on optimizing a convex function involving l_1-norms) as proposed by Lustig and co-workers [11]. Each image was also constructed from four sub-images acquired with increasing phase encoding time, thus allowing quantification of the water content in the image via appropriate signal relaxation analysis. This imaging protocol is repeated a number of times during the moisture absorption process.

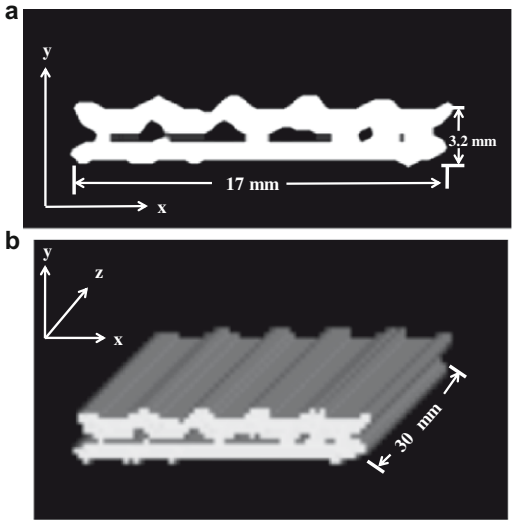

Fig. 1. (a) 2D and (b) 3D binary MR images of the wafer sheet with dimensions shown. The co-ordinate system shown is used for all image acquisitions.

2. Method development

2.1. Compressed sensing in MRI

Acquiring all the ***k***-space points or Fourier coefficients of a MR image is time consuming. Under-sampled ***k***-space acquisition is the method of choice when neither the spatial resolution nor the number of averages can be compromised for a desired SNR. From the Nyquist sampling theorem, we expect that when ***k***-space is strongly under-sampled, linear recovery methods will lead to lossy recovery and exhibit artefacts. It is important to note, however, that not all of the Fourier coefficients are equally important for the reconstruction of the image.

Recently compressed sensing [11,12] has attracted interest in terms of MR imaging. This sampling method takes advantage of the sparsity of MR images and allows good reconstructions from significantly under-sampled ***k***-space. A signal is described as sparse if it contains only a small number of non-zero values, or if these values decay very fast. We consider a transform domain sparsity, where the signal is not sparse but it can be manipulated to be in some transform domain. In the current context we make use of the acquired signal in the ***k***-space domain, this is transformed into the image domain and we exploit sparsity in a transform domain. Note that the image domain can be used as the transform domain if it presents sufficient sparsity. Lustig et al. [11,12], studied the exploitation of sparsity of MR images; for example they considered angiograms which have sparsity in the image domain. Many other types of 'natural' images (e.g., natural scenes, astronomical images) can exhibit sparsity in terms of their Fourier or wavelet coefficients, or in terms of discrete gradients; hence in their transform domain. The idea of taking advantage of sparsity in order to under-sample a signal is motivated by the success of image compression techniques. 'Natural' images and MR images can thus be compressed significantly with minimal loss of information. Several transforms can be used in order to transform an image to a sparse domain – e.g., the discrete cosine transform (DCT) as well as the wavelet transform are the basis for compression tools JPEG and JPEG-2000 [13].

Since MR images are compressible, compressed sensing theory [10,14] suggests that taking fewer acquisition samples, combined with prior knowledge that the image is sparse in the transform domain, may be sufficient for an accurate image reconstruction. This is achieved using a non-linear reconstruction method based on optimizing a convex function involving l_1-norms, related to the basis pursuit method [10]. In their work Lustig et al. [11] developed a framework for using CS in MRI, which has proved to be able to accurately reconstruct MR images from a small subset of ***k***-space rather than the entire ***k***-space grid.

2.2. Quantitative single point imaging with optimised sampling trajectory

A comprehensive study of a near optimum sampling scheme has been presented in previous work [9], where the sampling trajectory is dictated and ranked by the expected magnitude of the sampled ***k***-space points which we predict based on available prior knowledge of the sample shape. ***k***-Space points are sorted from maximum to minimum expected modulus signal intensity and divided into interleafs consistent with the centric scan sampling practise [8,15]. The principle used here is that ***k***-space points with the highest expected signal intensity are acquired with the highest value of magnetization. A time interval of $5 \times T_1$ is allowed between each interleaf to allow the magnetization to fully recover. As has been demonstrated in our previous study [9] a significant

improvement in the SNR and image quality can be achieved by following this sampling scheme.

The sampling strategy is based on the fact that SPI is a transient magnetization imaging method. This means that the magnetization will reduce from an initial value of M_0 to an equilibrium value after a certain number of pulse-acquire repetitions [16]. Without any magnetization preparation the magnetization available for imaging after the n^{th} excitation pulse-acquire repetition, M_n, is:

$$M_n = M_0(1-w)C^nE^n + M_0w \tag{1}$$

where $E = \exp(-TR/T_1)$, $C = \cos(\alpha)$ and $w = \frac{1-E}{1-CE}$. TR is the time between two successive excitation pulses and α is the r.f. pulse tip angle. In conventional SPI [5] where $\boldsymbol{k}$-space is sampled in a rectilinear trajectory, magnetization is saturated when at the extremities of $\boldsymbol{k}$-space and the remaining $\boldsymbol{k}$-space points are sampled with the same magnetization. This results in a comparatively poor SNR, which is generally determined by the centre of $\boldsymbol{k}$-space, hence the preference for centric sampling trajectories which commence at the centre of $\boldsymbol{k}$-space. An additional advantage is that in a centric scan there is no T_1 weighting of the origin of $\boldsymbol{k}$-space and hence total image intensity is directly proportional to the concentration of the signal-bearing species [4,8,15,17].

The signal intensity, $S(\mathbf{r})$ at any point, $\mathbf{r}$, in a SPI image will be given (ignoring T_1 relaxation effects) by [5]:

$$S(r) \propto \rho(r)\exp\left(-\frac{t_p}{T_2^*(r)}\right)\sin(\alpha) \tag{2}$$

$\rho(\mathbf{r})$ is the local ^{1}H density (^{1}H NMR is used in this paper exclusively) and t_p is the phase encoding time. In cases where t_p is much shorter than T_2^*, $S(\mathbf{r})$ will be relatively unaffected by signal relaxation; however, if t_p is comparable or longer than T_2^*, the signal intensity is attenuated by relaxation effects. Acquisition of $S(\mathbf{r})$ at various values of t_p, however, allows us to calculate $T_2^*(\mathbf{r})$ using Eq. (2) and therefore produce a comparatively quantitative image of $\rho(\mathbf{r})$.

With the above sampling method (as presented in [9]), once the $\boldsymbol{k}$-space points have been ranked then a subset of them with the highest intensity can be acquired in a sparse $\boldsymbol{k}$-space sampling scheme. In order for this method to be used for compressed sensing, it is required that under-sampling causes incoherent artefacts, or more formally the sampling operator must not be easily (sparsely) represented in the transform domain [14]. It has been shown [18] that when a good knowledge of the signal exists, then the sampling of the signal should aim to acquire the coefficients with the highest expected intensity for optimal results in the CS framework. Knowledge of the wafer shape provides such prior knowledge. Fig. 2(a) shows a simulated 2D image of a wafer sample, whilst in Fig. 2(b) the magnitude of its corresponding $\boldsymbol{k}$-space is shown. The resultant selected $\boldsymbol{k}$-space points (20% of the highest expected intensity) are shown as a binary image in Fig. 2(c). Simulations using the sampling trajectory or pattern in Fig. 2(c) reveal no obvious coherent artefacts which indicate that this sampling trajectory is sufficiently incoherent.

Compressed sensing and SPI constitute a powerful combination as the use of only phase encoding means that all imaging dimensions can be under-sampled. By comparison conventional 2D frequency-phase-encoding imaging, as used by Lustig et al. [11], can only be usefully under-sampled in the phase dimension. In addition with respect to SPI, there are no constraints on the $\boldsymbol{k}$-space sampling trajectory.

2.3. Sparsifying transform and image reconstruction

The sparsifying transform that is used in our case study is spatial discrete gradients (i.e., it computes differences of neighbouring pixels). We compute both the horizontal and the vertical gradients.

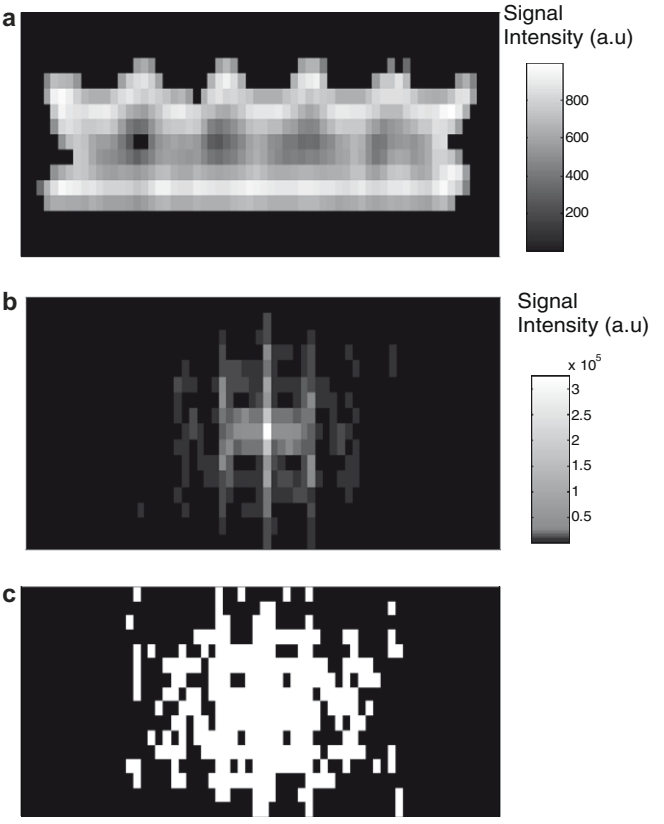

Fig. 2. (a) Typical 2D image of a wafer sample (b) $\boldsymbol{k}$-space modulus map (c) our sampling trajectory employed to acquire 20% of the highest intensity $\boldsymbol{k}$-space points.

Such a linear transform increases the dimension of the transform space, i.e., the number of coefficients roughly doubles. However, away from the boundaries of the object in the image these pairwise differences will be small or close to zero. Only right on the boundaries will the coefficients be significant. Thus spatial finite differences is appropriate for our piecewise smooth images and only a small percentage of the transform coefficients is sufficient for an accurate, and in our case, sufficiently quantitative reconstruction. To confirm this, we considered typical 3D images of the wafer; both a dry and a 15 wt% moisture sample. Fig. 3 shows the descending rank order of the coefficients in the Finite Difference transform domain. It is clear that the energy (signal intensity) of these coefficients is predominately contained in a small subset and thus that finite differences sparisfy this particular system well. The distribution is only slightly broader for the wet sample, indicating that the finite difference approach is fine for all the scenarios we considered. It may in future be possible to have an even better sparsifying transform by designing one directly for the images of interest [19]. This will potentially reduce the number of required $\boldsymbol{k}$-space measurements further.

Typically in SPI, $\boldsymbol{k}$-space is sampled one point per acquisition using an appropriate combination of phase-encoding gradients. To improve the efficiency of single point imaging techniques, Balcom and co-workers have proposed the acquisition of multiple points of the FID [20–22], which can be co-added to increase the SNR. These points, at increasing temporal locations along the FID, however, correspond to increasing $\boldsymbol{k}$-space co-ordinates and effectively a shrinking field of view (FOV). Rescaling to the same FOV is achieved via use of the chirp z-transform [20]. When the difference in phase encode time between the successive images is kept to a minimum (as dictated by hardware restrictions), then the FOV

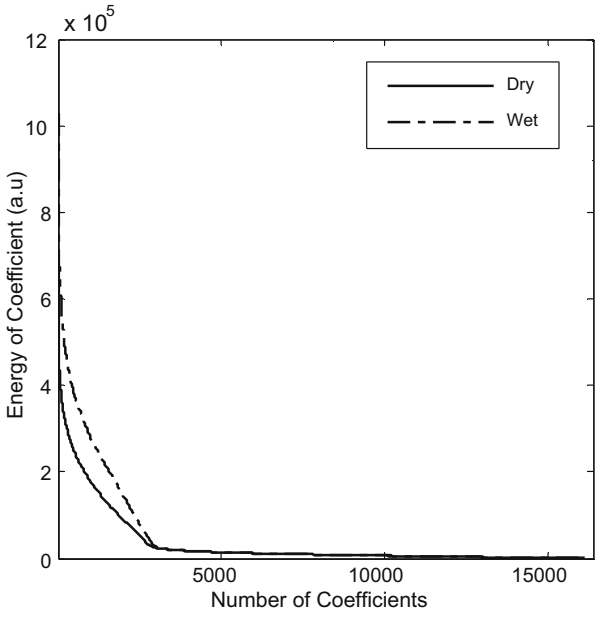

Fig. 3. Descending rank order of discrete gradient coefficients of typical 3D images of both a dry wafer and a wet wafer (15 wt%).

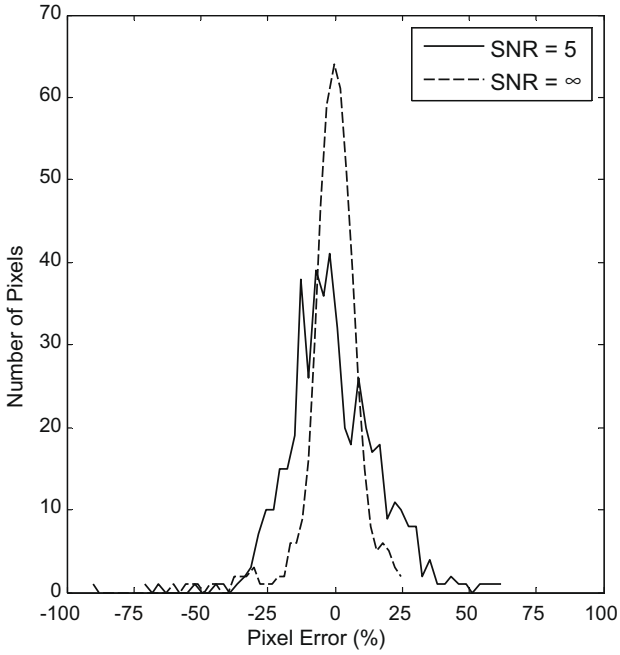

Fig. 4. Histograms of pixel error (%) resulting from the reconstructed image – original image for both SNR = ∞ and SNR = 5.

change between the successive images is minimal and the images retain all the geometrical characteristics and can hence be sparsified by the same transform.

The image reconstruction method that we use in our study is based on solving a convex optimization problem involving l_1-norms, a variant of basis pursuit [10,11]. If an image that we want to reconstruct is stacked as a vector $\boldsymbol{m}$, Ψ is the operator that transforms from pixel representation to a sparse representation, $\boldsymbol{F}$ is the under-sampled Fourier transform to $\boldsymbol{k}$-space and y are the $\boldsymbol{k}$-space measurements. The reconstruction is then obtained by solving the following constrained optimization problem:

$$\begin{aligned} &\min||\Psi m||_1 \\ &s\cdot t||Fm-y||_2<\varepsilon \end{aligned} \tag{3}$$

where ε is a threshold that can be set to the expected noise level. The l_1-norm acts as a proxy for sparsity – i.e., minimising the above objective produces an image which has the sparsest representation in the transform domain while remaining consistent with acquired measurements. The objective function is minimised using projected conjugate gradients following the approach of Lustig et al. [11]. Since the objective is convex, the algorithm finds the global minimum in the function. The reconstruction involving the l_1-norm is known to be a biased estimator for some systems, with the bias becoming more significant at lower SNR [23]. This bias appears in the sparse domain, so it could affect the reconstructed images in complex ways. A debiasing scheme such as the one in [23] could be used. Here we consider the bias and error of the reconstruction using appropriate simulations. The image of the wafer in Fig. 2(a) was reconstructed using our methodology applied to 20% of the highest intensity $\boldsymbol{k}$-space coefficients. This was done with no measurement noise added (SNR = ∞) and with the addition of Gaussian measurement noise to both the real and imaginary components (SNR = 5, note this ratio corresponds to the lowest SNR of the various acquired images presented later). The % error between the reconstructed images and the original images was calculated for each pixel, the corresponding data is presented as pixel histograms of % error in Fig. 4. In both cases the error is centred around 0 and the bias towards a negative error is relatively small. In the case of no measurement noise (SNR = ∞) the mean of the error is only −1.1%, which is very small. In the case of SNR = 5, the distribution of error is larger, consistent with the poorer SNR, but the mean of the error is still only −2.3%, which again is relatively small.

2.4. Experimental setup

All experiments were conducted using a Bruker AV400 spectrometer equipped with a micro-imaging r.f. coil of 25 mm internal diameter. Food wafer samples, binary gated 2D cross-sectional and 3D MR images of which are shown in Fig. 1, were placed in a 17 mm internal diameter NMR tube featuring a glass sample holder and connected to a humidified air source (18.6 ± 0.5 °C; relative humidity >95%) at a flow rate of 250 ml min^{-1}. The 3D SPI pulse sequence used is schematically shown in Fig. 5 (single interleaf shown). Each image consisted of four successive sub-images, each acquired with a different range of phase encoding time (and hence a reduced applied gradient strength to ensure a consistent FOV), in order to quantify the water content. As shown in Fig. 5, for each $\boldsymbol{k}$-space 'point', five points of the FID were acquired separated by a dwell time of 1 μs. For the first sub-image these corresponded to phase encoding times of 76, 77, 78, 79 and 80 μs. The second sub-image used phase encode times from 96 to 100 μs, the third from 116 to 120 μs and the fourth from 136 to 140 μs, respectively. Exceeding this 5 μs range resulted in image artefacts in the co-added images reconstructed with the same FOV via the chirp z-transform, this effect was made more acute by the presence of sharp edges in our sample. These images were first reconstructed individually through the optimization scheme that was described earlier and then co-added to improve the SNR.

All images were acquired using a tip angle of 3° corresponding to a pulse duration of 3 μs, and a repetition time (T_R) of 2 ms. The images were acquired over a field of view of $2\times1\times5$ cm^3 and consisted of $64\times32\times8$ pixels. For these under-sampled (33% acquired) images, followed by compressed sensing reconstruction, 5400 pulse-acquire events were required (split into 8 interleafs of 675 points), which with four signal averages and the acquisi-

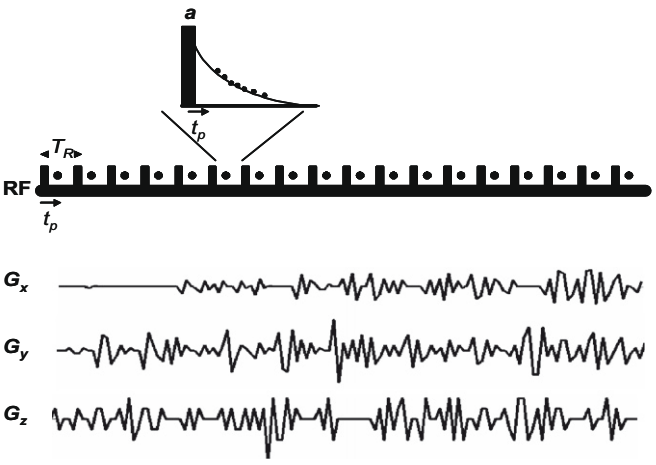

Fig. 5. 3D SPI pulse sequence, a single interleaf is shown. A broadband r.f. pulse excites transverse magnetization which is phase encoded for time, t_p. Multiple complex points [•] are acquired at every gradient (G_x, G_y, G_z) step increase for signal averaging. The repetition time, defined by the time between two successive r.f. pulses is *TR*. A typical gradient (and hence ***k***-space) trajectory is shown.

tion of four sub-images resulted in a total acquisition time of 13 min.

3. Results and discussion

3.1. Improvement due to compressed sensing reconstruction

Using a typical 3D image of the wafer material, full images were constructed as a function of the percentage of expected highest intensity ***k***-space or Fourier coefficients retained, using the sampling trajectory described above. In each case the average (absolute magnitude) pixel error was calculated with reference to the reconstructed image with full ***k***-space sampling. The result is shown in Fig. 6. It is evident that by acquiring only 33% of the ***k***-space points followed by a compressed sensing reconstruction, the average error is kept below 3%. For this calculation, only pixels from within the object of interest are considered. This translates to a possible 66% reduction in total acquisition time. For comparison in Fig. 6, the average pixel error as a function of ***k***-space sampled is shown for the case of zero-filling un-sampled data followed by conventional Fourier transform. Fig. 6 clearly demonstrated the superior performance of compressed sensing.

3.2. Quantification of moisture content

NMR experiments on samples such as crystals and glasses often show a beat or oscillation in their free induction decay (FID) [24]. This beat has been observed in dry food systems as well [25–28]. The beat arises from residual order within the sample resulting from regular spacing between neighbour protons that give rise to dipolar spectral line shape, also referred as the 'Pake pattern' [29,30]. In such materials the observed FID is a superposition of the FIDs of the mobile and the immobile protons [24]. Signal arising from the liquid decays in a simple exponential fashion. Decay of the 'solid' signal is described by a composite of a Sinc function and Gaussian broadening. The signal intensity of the FID, $S_{\mathrm{obs}}(t)$, can therefore be expressed as:

$$S_{\mathrm{obs}}(t) = A_S \exp\left(-\frac{1}{2}a^2t^2\right)\frac{\sin bt}{bt} + A_L \exp\left(-\frac{t}{T_{2L}^*}\right) \tag{4}$$

A_S is the population of immobile ^{1}H, α is the inverse of the standard deviation of the Gaussian function, b is the angular frequency of the Sinc function and A_L is the population of the mobile ^{1}H. The second moment M_2 of the acquired line shape is a measure of the strength of the dipolar interactions [24,25] and is given by:

$$M_2 = a^2 + \frac{1}{3}b^2 \tag{5}$$

Typical FIDs of the wafer at different moisture levels are shown in Fig. 7 together with the fit of Eq. (4). For this experimental series the wafer samples where initially dried to a moisture content of 2 wt%, this remaining water is bound in the starch matrix. Humidified air was then blown over the sample *ex situ* and an FID acquired periodically. The total moisture uptake was determined gravimetrically immediately prior to each FID acquisition. At the end of the experiment the final moisture content was also determined using a Sartorius MA-45 moisture analyser. The quality of fit in Fig. 7 is excellent for comparatively low moisture contents and then deteriorates slightly as moisture content increases. As observed by others [24] for similar samples, this probably originates from a multi-exponential behaviour of the mobile proton signal or more likely spatial variations in moisture content (which will be significantly reduced when imaging). Nevertheless, with reference to Fig. 7, a single exponential provides a reasonable fit for moisture contents of 15 wt% or less; this covers the range of industrial interest.

Fig. 8(a) and (b) show the evolution in T_{2L}^*, A_L and A_S, respectively, with total moisture content. With reference to Fig. 8(b), an approximately linear relationship is observed between moisture content and A_L, which with reference to Eq. (2) is required for quantitative moisture mapping. A_S remains relatively constant as

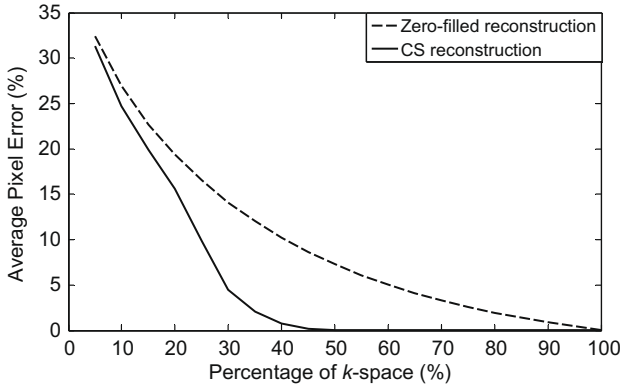

Fig. 6. Plot of the average pixel error as a percentage of ***k***-space sampled. Reconstruction is by either compressed sensing (*CS*) or by conventional zero-filling followed by Fourier transform. The superiority of CS is distinct.

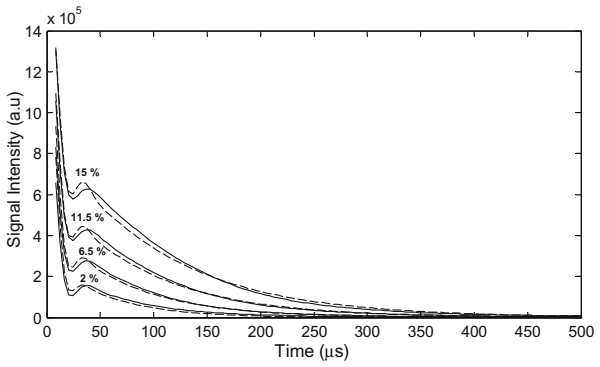

Fig. 7. Sample FIDs of wafer samples (humidified *ex situ*) at moisture contents of ~2, 6.5, 11.5 and 15 wt% moisture content are shown by the solid lines. The corresponding fits of Eq. (4) are shown by the dashed lines.

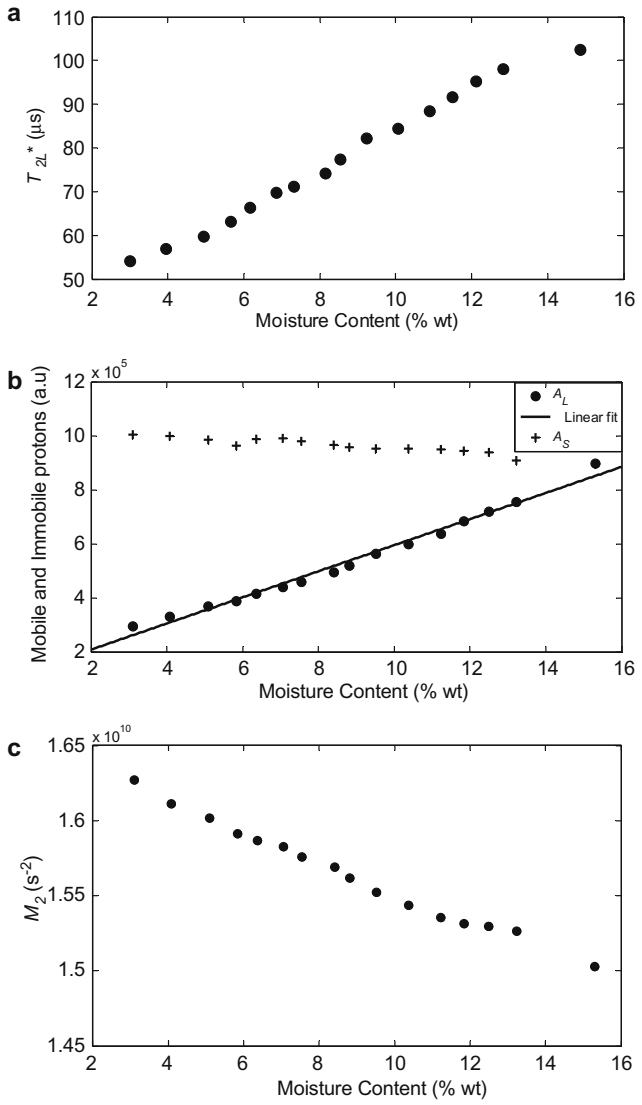

Fig. 8. The dependency of (a) T_2^*, (b) A_L, mobile and A_s, immobile ^{1}H signal (as determined from FID acquisition of *ex situ* humidified samples) on bulk moisture content. The relationship between A_L, and bulk moisture content is approximately linear. (c) Second moment of the acquired line shape as a function of moisture content, determined using Eq. (4).

expected, the slight decrease probably results from some increased mobility of the starch structure with increased moisture content. This is consistent with a slight decrease in the second moment of the line shape (M_2) as shown in Fig. 8(c), calculated using the fit parameters and Eq. (5). There is an offset at zero moisture content suggesting a small inherent contribution to the mobile proton signal from other constituents of the wafer such as mobile fats and lipids. The observed increase in T_{2L}^* with moisture content in Fig. 8(a) is as expected and indicates that the water is becoming increasingly mobile as its content is increased. In all imaging experiments conducted, the minimum phase encoding time was 75 μs. Analysis of the FIDs using Eq. (4) indicates the signal contribution from the immobile ^{1}H to the acquired image intensity, $S_{obs}(t)$, when $t = 75$ μs is consistently less than 0.1% and hence can be ignored. Thus for our *in situ* wafer humidification experiments, we are able to quantify our bulk moisture content as a function of time via the periodic acquisition of FIDs and using Fig. 8(b). The resultant evolution of total moisture content with time is shown in Fig. 9. The full analysis of the FID was performed in order to guarantee that the signal from the solids components is not significant at the phase encode times used here. If a full analysis of the solid and liquid composition of the individual pixels is required then images at shorter phase encode times need to be acquired [31]. In our case, due to gradient strength restrictions, we are not able to acquire at such short phase encode times.

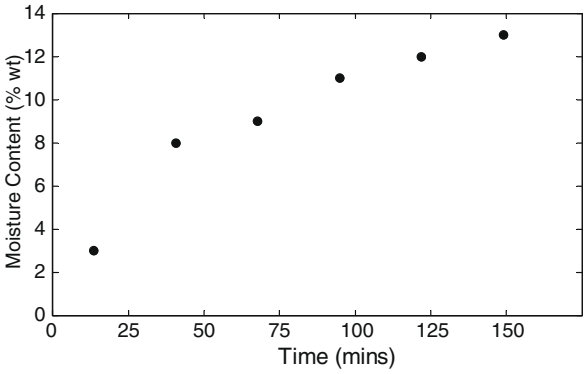

Fig. 9. Bulk moisture content of the wafer sample, humidified *in situ*, as extracted from the FID measurements as a function of time.

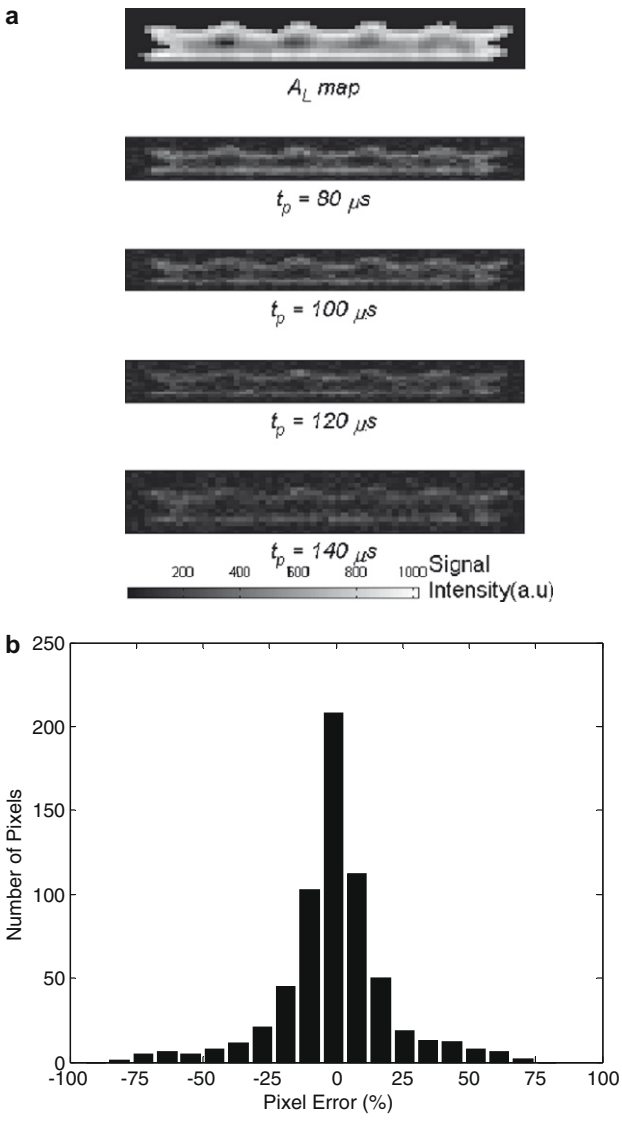

Fig. 10. (a) A_L map and simulated images at different phase encode times with measurement noise added. (b) Histogram of the pixel error (%) with respect to A_L.

3.3. Expected propagation of errors

In order to recover the quantitative moisture content maps, as described previously, the T_2^* relaxation effects need to be reversed in each pixel and the signal hence extrapolated to the origin of time when it is proportional to the moisture content. This back extrapolation is achieved by fitting a single exponential decay to the data for each pixel. Potential sources of error include measurement noise, the effects of under-sampling ***k***-space and the reconstruction optimization routine used. As shown in Fig. 4, the effects of under-sampling and reconstruction is an insignificantly small bias. In order to consider the propagation of error from these original sources, the following simulation was performed: Fig. 2(a) was assigned to be the moisture map at time zero (i.e., a map of A_L). Typical T_2^* values were assigned to each pixel and the images at different phase encode times (as were used in all image acquisitions) were produced with Gaussian noise added to both the real and imaginary components in the image domain. The resultant series of images are presented in Fig. 10(a). The SNR was 5:1 (the lowest encountered experimentally) in the lowest intensity image. Each image was reconstructed using 33% of the highest expected intensity ***k***-space coefficients. A single exponential was fitted to each pixel to recover a map of A_L. A histogram of the resultant % error in A_L is presented in Fig. 10(b). This is clearly centred on zero with minimal bias and >93% of the pixels presenting an error less than 10%.

3.4. Three dimensional imaging

3D SPI images of the wafer sample were acquired periodically during the humidification process. Using the appropriately truncated form of Eq. (4) applied to the four sub-images and the data in Fig. 8(b), these were converted into quantitative moisture distribution images. As mentioned previously the total acquisition time of each quantitative 3D image was 13 min; with reference to Fig. 9 this was broadly consistent with the moisture absorption kinetics displayed by the wafer. A fully sampled equivalent SPI image would require a total acquisition time of approximately 39 min. With reference to Fig. 7, to produce an identical average pixel error when employing zero-filling and conventional Fourier Transform would require acquisition of 75% of the ***k***-space points and a total acquisition time of approximately 30 min.

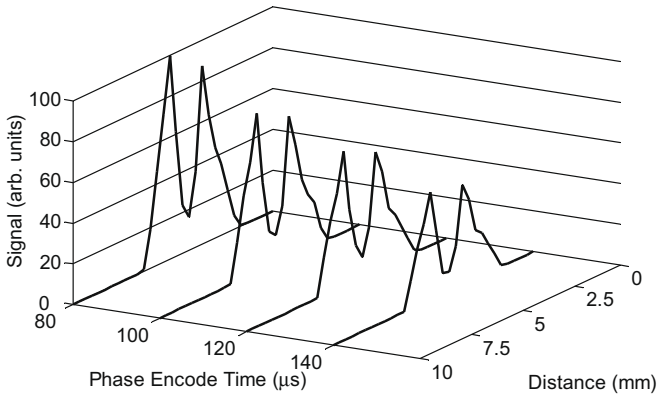

Fig. 11. Sample attenuation of the signal in a 1D profile extracted from an *x*–*y* image for each of the four sub-images at increasing phase encode time.

Fig. 11 shows extracted signal profiles from the four sub-images across the thinnest dimension of the wafer; the decrease in signal with phase encoding time due to T_2^* relaxation is evident. From the series of four sub-images acquired at different phase encoding intervals, T_2^* and A_L maps were generated using Eq. (4). We are effectively extrapolating back to a phase encoding time of 0 ms when determining the A_L maps. Fig. 12 shows the T_2^* maps of a central slice of the 3D image as a function of bulk moisture content. Initially, increases in T_2^* occur preferentially near the surface of the wafer, with further moisture absorption resulting in an increase in T_2^* towards the centre of the sample. Extrapolated and hence quantitative moisture maps are shown for the same slice in Fig. 13(a). Initially in the driest image, local 'spikes' in moisture content are observed. In subsequent images the moisture absorption starts from the surface pixels, as was qualitatively seen in the T_2^* maps, whilst for the last two acquisitions the moisture content appears relatively homogeneous across the sample. Fig. 13(b) shows the extracted 1D profiles of moisture content from the slices presented in Fig. 13(a).

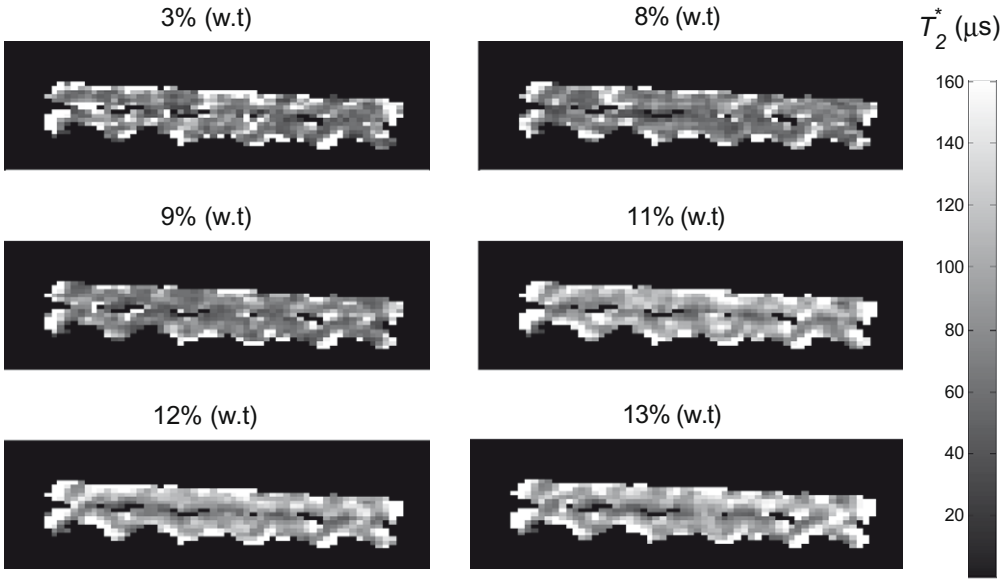

Fig. 12. T_2^* maps of a central slice of the 3D images, obtained after fitting Eq. (4) to each pixel using the four sub-images reconstructed using the compressed sensing method described in the text. These are shown as a function of bulk moisture content.

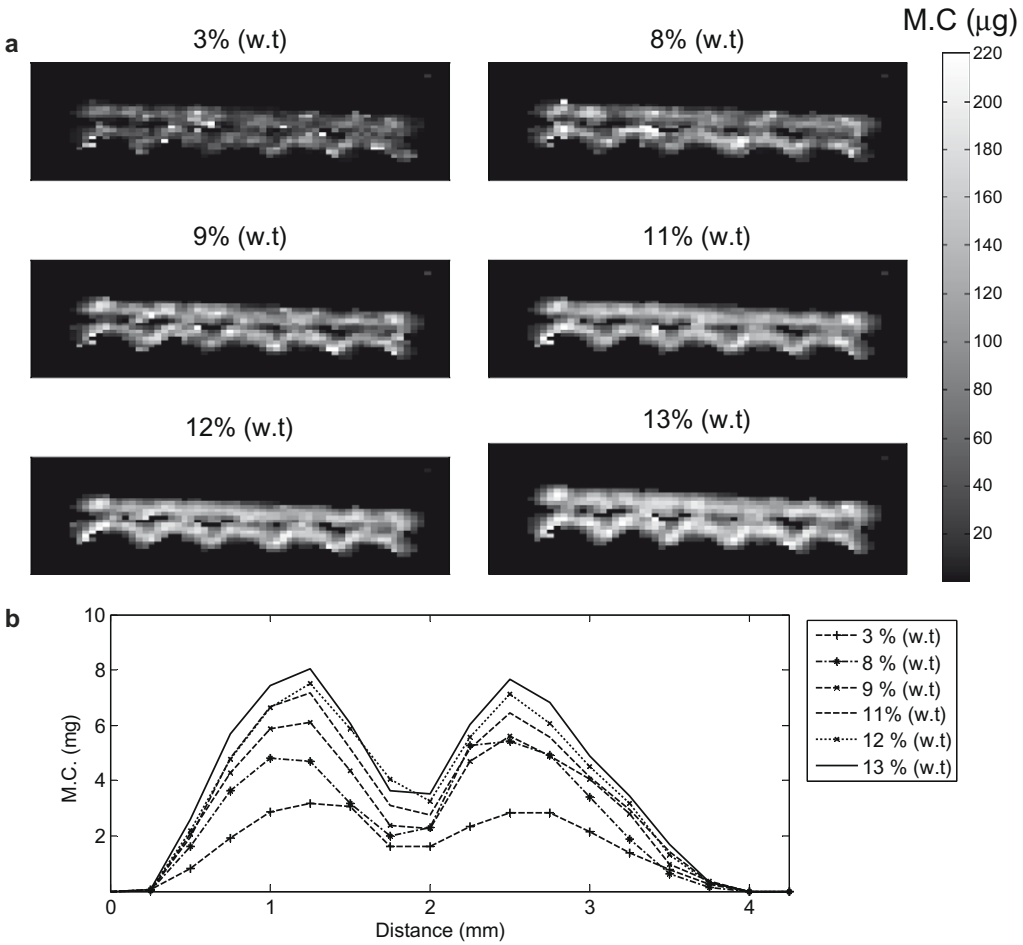

Fig. 13. (a) Quantitative moisture distribution maps (taken from the 3D images), obtained after fitting Eq. (4) to each pixel using the four sub-images reconstructed using the compressed sensing method described in the text. These are shown as a function of bulk moisture content (b) 1D profiles extracted from the 2D slices in (a).

4. Conclusion

We have presented several improvements to the SPI technique aimed primarily at increasing its temporal resolution. This is conducted using 3D imaging of the conditioning of a wafer system in a humidified environment as a case study. The most significant improvement is the use of compressed sensing to effect image reconstruction; which improves accuracy of the images significantly when under-sampling ***k***-space; a mean pixel error of only 3% is produced when sampling only 33% of ***k***-space in each image. SNR is improved via multiple point acquisition and subsequent FOV correction using a chirp *z*-transform, whilst quantitative moisture distribution is recovered via appropriate analysis of a series of sub-images acquired at different phase encode time intervals. The back extrapolation results in an unbiased quantitative recovery of the water signal.

Acknowledgments

The financial support of Nestlé, Microsoft and a Case Award from the BBSRC is acknowledged.

References

[1] S. Emid, Ultra high-resolution multiple quantum spectroscopy in solids, Physica B, C 128 (1985) 79–80.
[2] S. Emid, J.H.N. Creyghton, High-resolution imaging in solids, Physica B, C 128 (1985) 81–83.
[3] S.D. Beyea, B.J. Balcom, I.V. Mastikhin, T.W. Bremner, R.L. Armstrong, P.E. Grattan-Bellew, Imaging of heterogeneous materials with a turbo spin echo single-point imaging technique, J. Magn. Reson. 144 (2000) 255–265.
[4] I.V. Mastikhin, H. Mullally, B. MacMillan, B.J. Balcom, Water content profiles with a 1D centric SPRITE acquisition, J. Magn. Reson. 156 (2002) 122–130.
[5] S. Gravina, D.G. Cory, Sensitivity and resolution of constant-time imaging, J. Magn. Reson. Ser. B 104 (1994) 53–61.
[6] B.J. Balcom, R.P. MacGregor, S.D. Beyea, D.P. Green, R.L. Armstrong, T.W. Bremner, Single-point ramped imaging with T-1 enhancement (SPRITE), J. Magn. Reson. Ser. A 123 (1996) 131–134.
[7] M. Halse, D.J. Goodyear, B. MacMillan, P. Szomolanyi, D. Matheson, B.J. Balcom, Centric scan SPRITE magnetic resonance imaging, J. Magn. Reson. 165 (2003) 219–229.
[8] A.A. Khrapitchev, B. Newling, B.J. Balcom, Centric-scan SPRITE magnetic resonance imaging with prepared magnetisation, J. Magn. Reson. 181 (2006) 271–279.
[9] P. Parasoglou, A.J. Sederman, J. Rasburn, H. Powell, M.L. Johns, Optimal *k*-space sampling for single point imaging of transient systems, J. Magn. Reson. 194 (2008) 99–107.
[10] D.L. Donoho, Compressed sensing, IEEE Trans. Inf. Theory 52 (2006) 1289–1306.
[11] M. Lustig, D. Donoho, J.M. Pauly, Sparse MRI: the application of compressed sensing for rapid MR imaging, Magn. Reson. Med. 58 (2007) 1182–1195.
[12] M. Lustig, D.L. Donoho, J.M. Santos, J.M. Pauly, Compressed sensing MRI, IEEE Signal Proc. Mag. 25 (2008) 72–82.
[13] D.S. Taubman, M.W. Marcellin, JPEG2000: standard for interactive imaging, Proc. IEEE 90 (2002) 1336–1357.
[14] E.J. Candes, J. Romberg, T. Tao, Robust uncertainty principles: exact signal reconstruction from highly incomplete frequency information, IEEE Trans. Inf. Theory 52 (2006) 489–509.
[15] A.A. Khrapitchev, B. Newling, B.J. Balcom, Sectoral sampling in centric-scan SPRITE magnetic resonance imaging, J. Magn. Reson. 178 (2006) 288–296.
[16] I.V. Mastikhin, B.J. Balcom, P.J. Prado, C.B. Kennedy, SPRITE MRI with prepared magnetization and centric *k*-space sampling, J. Magn. Reson. 136 (1999) 159–168.
[17] Q. Chen, M. Halse, B.J. Balcom, Centric scan SPRITE for spin density imaging of short relaxation time porous materials, Magn. Reson. Imaging 23 (2005) 263–266.

[18] Y. Weiss, H.S. Chang, W.T. Freeman, Learning compressed sensing, in: 45th Allerton Conference on Communication, Control, and Computing, Monticello, IL, USA, 2007.
[19] M. Aharon, M. Elad, A. Bruckstein, K-SVD: Design of Dictionaries for Sparse Representations, SPARS, Rennes, France, 2005.
[20] M. Halse, J. Rioux, S. Romanzetti, J. Kaffanke, B. MacMillan, I. Mastikhin, N.J. Shah, E. Aubanel, B.J. Balcom, Centric scan SPRITE magnetic resonance imaging: optimization of SNR, resolution, and relaxation time mapping, J. Magn. Reson. 169 (2004) 102–117.
[21] J. Kaffanke, T. Dierkes, S. Romanzetti, M. Halse, J. Rioux, M.O. Leach, B. Balcom, N.J. Shah, Application of the chirp *z*-transform to MRI data, J. Magn. Reson. 178 (2006) 121–128.
[22] A.J. Rioux, A.M. Halse, A.E. Aubanel, A.B.J. Balcom, A.J. Kaffanke, A.S. Romanzetti, A.T. Dierkes, A.N.J. Shah, An Accurate Nonuniform Fourier Transform for SPRITE Magnetic Resonance Imaging Data, vol. 33, ACM Press, 2007.
[23] M.A.T. Figueiredo, R.D. Nowak, S.J. Wright, Gradient projection for sparse reconstruction: application to compressed sensing and other inverse problems, IEEE J. Selected Top. Signal Proc. 1 (2007) 586–597.
[24] W. Derbyshire, M. van den Bosch, D. van Dusschoten, W. MacNaughtan, I.A. Farhat, M.A. Hemminga, J.R. Mitchell, Fitting of the beat pattern observed in NMR free-induction decay signals of concentrated carbohydrate–water solutions, J. Magn. Reson. 168 (2004) 278–283.
[25] I.J. van den Dries, D. van Dusschoten, M.A. Hemminga, E. van der Linden, Effects of water content and molecular weight on spin probe and water mobility in malto-oligomer glasses, J. Phys. Chem. B 104 (2000) 10126–10132.
[26] I.J. van den Dries, D. van Dusschoten, M.A. Hemminga, Mobility in maltose-water glasses studied with H-1 NMR, J. Phys. Chem. B 102 (1998) 10483–10489.
[27] B.P. Hills, K. Pardoe, Proton and deuterium NMR studies of the glass transition in a 10% water–maltose solution, J. Mol. Liquids 63 (1995) 229–237.
[28] H. Kumagai, W. MacNaughtan, I.A. Farhat, J.R. Mitchell, The influence of carrageenan on molecular mobility in low moisture amorphous sugars, Carbohydr. Polym. 48 (2002) 341–349.
[29] G.E. Pake, E.M. Purcell, Line shapes in nuclear paramagnetism, Phys. Rev. 74 (1948) 1184.
[30] I.J. Lowe, R.E. Norberg, Free-induction decays in solids, Phys. Rev. 107 (1957) 46.
[31] K. Deka, B. MacMillan, G.R. Ziegler, A.G. Marangoni, B. Newling, B.J. Balcom, Spatial mapping of solid and liquid lipid in confectionery products using a ID centric SPRITE MRI technique, Food Res. Int. 39 (2006) 365–371.